Two-dimensional MoTe2/SnSe2 van der Waals heterostructures for tunnel-FET applications

Two-dimensional $MoTe_2/SnSe_2$ van der Waals heterostructures for tunnel-FET applications

Konstantina Iordanidou* and Julia Wiktor
Department of Physics, Chalmers University of Technology, SE-412 96 Gothenburg, Sweden

(Received 17 January 2022; accepted 28 June 2022; published 5 August 2022)

Two-dimensional (2D) van der Waals heterostructures (vdWHs) are attractive candidates for realizing tunnel field-effect transistors (TFETs) for low-power applications. In this work, using first-principles calculations based on density functional theory (DFT), we explore heterostructures composed of 2D $MoTe_2$ and $SnSe_2$. Our calculations reveal that upon forming the heterostructures, the valence band top of $MoTe_2$ and the conduction band bottom of $SnSe_2$ are almost aligned, forming the nearly broken-gap or type-III band alignment which is highly promising for TFETs. Interestingly, we find that the band alignment can be tuned by applying external electric fields. For positive electric fields, $MoTe_2$ ($SnSe_2$) band-edge positions are shifted upward (downward) with respect to the Fermi level, and more electrons are expected to tunnel from $MoTe_2$ to $SnSe_2$. Overall, our simulations provide fundamental insights into the electronic properties of $MoTe_2/SnSe_2$ stacks, and pave the way for the design and fabrication of future $MoTe_2/SnSe_2$-based TFETs.

DOI: 10.1103/PhysRevMaterials.6.084001

I. INTRODUCTION

Over the past decades, the miniaturization of metal–oxide–semiconductor field-effect transistors (MOSFETs) resulted in significant improvement in power efficiency. However, further reduction of the MOSFET dimensions will lead to a dramatic increase in power consumption. The so-called "Boltzmann tyranny" limits the subthreshold swing (SS) at the minimum of 60 mV/dec at 300 K; i.e., to modulate the drain current by one order of magnitude, a gate voltage of at least 60 mV is required. This prevents from scaling down the power supply voltage as the physical dimensions of the MOSFET are reduced; to overcome this limitation, new transistor structures have emerged, like the tunnel field-effect transistor (TFET) [1–3].

Contrary to conventional MOSFETs where the charge carriers are injected over a potential barrier, in TFETs, conduction occurs through band-to-band tunneling. van der Waals heterostructures (vdWHs) composed of two-dimensional (2D) materials are highly promising for TFET applications. Their band alignments can be easily tuned through the gate, and their high-quality interfaces can eliminate the parasitic trap-assisted tunneling observed in conventional heterostructures. Furthermore, owing to the weak interlayer interaction, vdWHs do not demand the lattice match condition, and a variety of potential promising heterostructures can be constructed. Recently, TFETs based on $WSe_2/SnSe_2$ vdWHs with a minimum SS of 37 mV/dec, an on-off current ratio over 10^6, and a tunneling current over 10^{-5} A have been reported [4]. Although various vdWHs exhibiting band-to-band tunneling have been experimentally realized [4–8], the quest for optimal heterostructures is still an open issue.

Using first-principles calculations based on density functional theory (DFT), we examine the electronic properties of $MoTe_2/SnSe_2$ vdWHs, including the projected band structure, band alignment, and charge transfer. For the first time, the fundamental properties of $MoTe_2/SnSe_2$ heterobilayers are investigated in depth, and the heterobilayer is proposed as an attractive candidate for realizing ultraminiaturized tunneling transistors. In particular, we identified a combination of 2D materials which exhibits the nearly broken-gap or type-III band alignment, and the proposed 2D materials can be experimentally synthesized and are stable, contrary to other investigations focusing on hypothetical low-dimensional systems. In our work, we explored heterostructures composed of single-layer $MoTe_2$ and single-layer $SnSe_2$, and, due to quantum confinement effects, the electronic properties of single layers can be completely different compared to their few-layer counterparts.

II. METHODS

All DFT calculations were performed using the Vienna *ab initio* simulation package [9,10]. Projected augmented wave pseudopotentials were employed [11] with valence electron configurations of $4d^5\,5s^1$ for Mo, $5s^2\,5p^4$ for Te, $4d^{10}\,5s^2\,5p^2$ for Sn, and $4s^2\,4p^4$ for Se. For the atomic relaxations, we used the conjugate gradient method with 10^{-2} eV/Å force convergence criteria on the ionic optimization and 10^{-8} eV energy convergence criteria on the electronic minimization.

We constructed low-strained $MoTe_2/SnSe_2$ van der Waals heterostructures using the CellMatch code [12]. Periodic

*konstantina.iordanidou@chalmers.se

boundary conditions were applied, and a vacuum layer larger than 15 Å was inserted in the vertical direction to minimize spurious interactions between periodic images. For the atomic relaxations and total energy calculations, long-range van der Waals (vdW) corrections were included using the rev-vdW-DF2 functional [13], which has been found to describe weakly bound solids accurately [14], whereas for all other calculations the functional proposed by Perdew, Burke, and Ernzerhof (PBE) was adopted. In total, six van der Waals functionals were tested—namely, rev-vdW-DF2, Opt-B88, Opt-PBE, vdW-DF, vdW-DF2, and vdW-DF-cx [15–20]—and for rev-vdW-DF2, the computed lattice parameters of bulk $MoTe_2$ and $SnSe_2$ were closer to the experimental values [21,22] (see Supplemental Material Table S1 [23]).

The kinetic energy cutoff was set to 500 eV and the Brillouin zone was sampled by a $4 \times 4 \times 1$ k-point grid for the atomic relaxations, whereas a denser grid was used for the band structure calculations. The effect of spin-orbit coupling (SOC) on the electronic properties was also studied. In particular, using the rev-vdW-DF2 optimized structures, we computed the electronic properties by switching on SOC and by using the PBE functional [24]. To correct the underestimation of the band gap within DFT, we computed the band structures using the hybrid Heyd–Scuseria–Ernzerhof functional [25] along with the standard mixing parameter of 0.25.

To study the effect of external electric fields, dipole corrections were applied in the out-of-plane direction. In the absence of an external electric field, calculations with and without dipole calculations were performed. We found that dipole corrections resulted in an energy variation of only 0.06 meV/atom, whereas no noticeable changes in the electronic band structures were observed. Therefore, in the absence of an external electric field, dipole corrections were omitted.

III. RESULTS AND DISCUSSION

A. Structural and electronic properties of $MoTe_2/SnSe_2$ vdWHs

The relaxed atomic structures of single-layer $MoTe_2$ and $SnSe_2$ are shown in Fig. 1. Both materials consist of one hexagonal metal plane sandwiched between two hexagonal chalcogen planes. $MoTe_2$ has the trigonal prismatic coordination (1H phase), whereas $SnSe_2$ has the octahedral coordination (1T phase). For the optimized unit cells, the in-plane lattice constants are $a_{MoTe_2} = 3.53$ Å and $a_{SnSe_2} = 3.84$ Å for $MoTe_2$ and $SnSe_2$, respectively, which are in excellent agreement with previously reported theoretical calculations [26]. The lattice mismatch is calculated using the formula $[(a_{SnSe_2} - a_{MoTe_2})/a_{MoTe_2}] \times 100\%$, and it is found to be as high as ∼9%. Therefore low-strained heterostructures cannot be formed by simply stacking the single-layer unit cells. To minimize the strain, we performed rotations of $SnSe_2$ with respect to $MoTe_2$ ranging from 0 to 30°, and we searched for stacks with relatively small number of atoms and small strain. Among the constructed configurations, the selected stack consists of (4×4) $MoTe_2$ and $(\sqrt{13} \times \sqrt{13})$ $SnSe_2$ layers, where $SnSe_2$ is rotated by ∼14°, whereas $MoTe_2$ is kept fixed. In this model, $MoTe_2$ lattice constants remain unchanged whereas $SnSe_2$ accumulates the total strain, which is ∼2%, and such small strain is expected to have a small impact on the electronic properties. It is worth noting that for the selected stack, many translation operations have been performed. In particular, $SnSe_2$ was shifted along the a and b directions using displacement intervals of $0.2a$ and/or $0.2b$. For each step, we performed atomic relaxations, and the energy difference between the highest and the lowest energy configurations was found to be only 0.01 meV/atom, indicating that the studied structures were energetically degenerate. For the sake of completeness, low-strained heterostructures with different rotation angles were also considered.

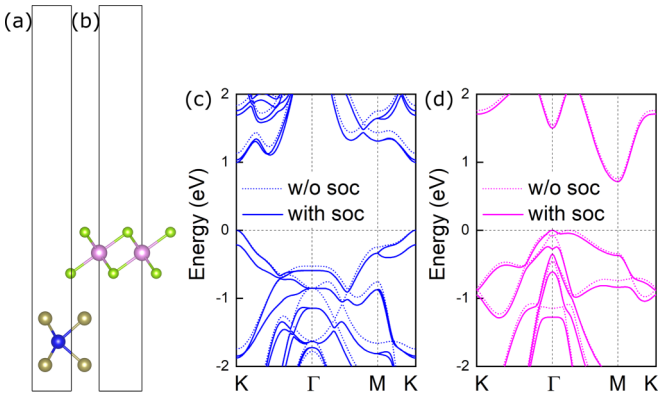

FIG. 1. Atomic structures and electronic band structures at the PBE level with and without SOC of single-layer $MoTe_2$ (a), (c) and $SnSe_2$ (b), (d) unit cells. The blue and brown spheres correspond to Mo and Te atoms, whereas the pink and green spheres correspond to Sn and Se atoms, respectively. The energies refer to the valence band maximum.

Next, to evaluate the structural stability of the heterostructure, we calculate its binding energy using the formula

$$E_b = E_{tot}(MoTe_2/SnSe_2) - E_{tot}(MoTe_2) - E_{tot}(SnSe_2), \quad (1)$$

where $E_{tot}(MoTe_2/SnSe_2)$, $E_{tot}(MoTe_2)$, and $E_{tot}(SnSe_2)$ are the total energies of the heterostructure, the isolated $MoTe_2$ layer, and the isolated (low-strained) $SnSe_2$ layer, respectively. The binding energy is found to be about -15 meV/Å^2, and the negative value indicates structural stability. Typical van der Waals bonded materials, like graphite and bulk MoS_2, present comparable binding energies (-12 meV/Å^2 for graphite [27] and -26 meV/Å^2 for bulk MoS_2 [28]). Therefore, we confirm that the interactions between the $MoTe_2$ and $SnSe_2$ layers are dominated by long-range van der Waals forces.

Using PBE calculations and taking into account SOC, the unit cell of $MoTe_2$ has a direct band gap of 1.00 eV whereas the unit cell of $SnSe_2$ exhibits an indirect band gap of 0.71 eV. Calculations without SOC result in slightly larger band gaps of 1.13 and 0.76 eV for $MoTe_2$ and $SnSe_2$, respectively, in agreement with previously reported theoretical calculations [29,30]. Figure 2 shows the electronic band structure of $MoTe_2/SnSe_2$ vdWHs, and the band alignment of the $MoTe_2$ and $SnSe_2$ layers with respect to the vacuum level before and after forming the heterostructure. Note that the

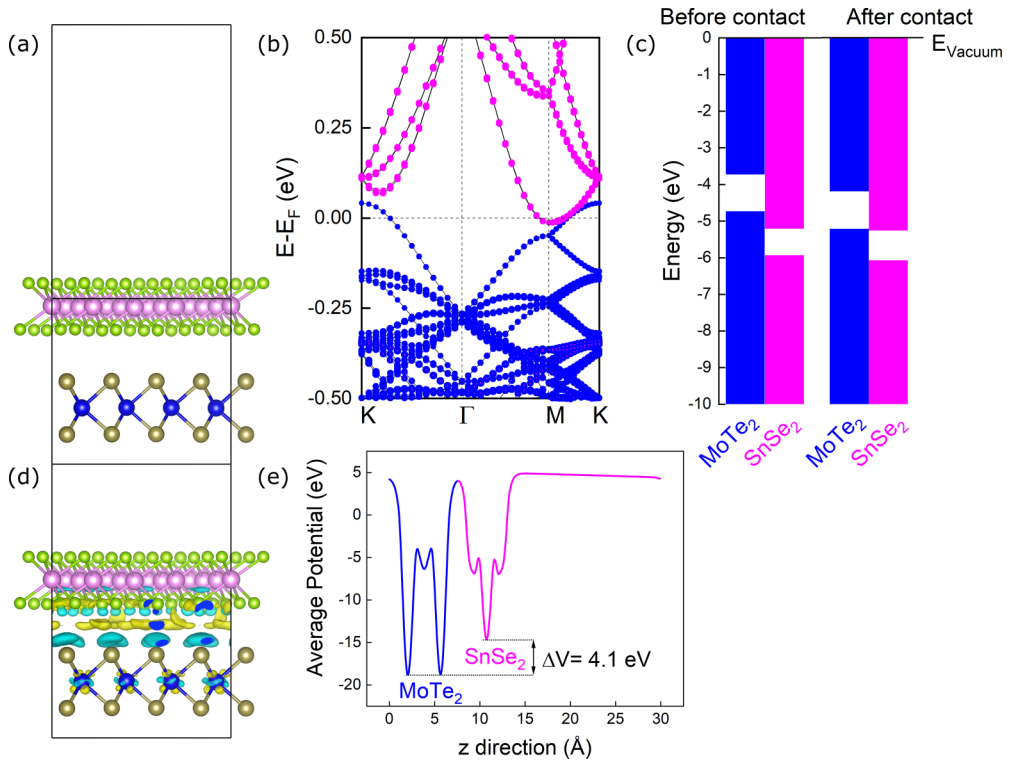

FIG. 2. (a), (b) Atomic structure and electronic band structure at the PBE level of $MoTe_2/SnSe_2$ vdWHs. (c) Schematic illustration of the band alignment of $MoTe_2$ and $SnSe_2$ before and after forming the heterostructure. (d), (e) Charge density difference $\Delta\rho_c = \rho(MoTe_2/SnSe_2) - \rho(MoTe_2) - \rho(SnSe_2)$ and average electrostatic potential along the z-axis. For the charge density difference, yellow and blue isosurfaces refer to electron accumulation and depletion, respectively, and the isosurface value is 0.0004 electrons/Bohr^3. SOC is included in the calculations.

band alignment before contact refers to the strain-free unit cells consisting of three atoms. The band structure of the heterostructure can be considered as a rough summation of the corresponding band structures of the isolated $MoTe_2$ and $SnSe_2$ layers. Interestingly, the conduction band (CB) bottom is located slightly below the Fermi level whereas the valence band (VB) top lies slightly above the Fermi level. The energy difference between the CB minimum originated from $SnSe_2$ and the VB maximum originated from $MoTe_2$ is -0.05 eV. Using PBE calculations without SOC, the energy difference is found to be -0.03 eV, i.e., only slightly higher compared to the calculations including this relativistic interaction. Since standard DFT significantly underestimates the band gaps, hybrid functional calculations are additionally performed. Due to the high computational cost, for hybrid functional calculations SOC is neglected. Concerning the electronic properties of the unit cells, $MoTe_2$ and $SnSe_2$ exhibit a band gap of about 1.57 and 1.41 eV, respectively. Despite the gap opening, the band alignment of the heterostructure is very similar to the results obtained from standard DFT, and the energy difference between the $SnSe_2$ CB bottom and the $MoTe_2$ VB top is 0.07 eV. By including SOC, a small decrease in the energy difference is expected. Remarkably, we find that the $MoTe_2/SnSe_2$ heterostructure presents the nearly broken-gap or type-III band alignment, which is highly promising for TFET applications.

Since the work function of monolayer $MoTe_2$ is lower compared to that of monolayer $SnSe_2$ [29], electrons will spontaneously move from $MoTe_2$ to $SnSe_2$ upon forming the heterostructure. As a result, the Fermi level of $MoTe_2$ and $SnSe_2$ will shift downward and upward, respectively, until they are aligned. The work function of the heterostructure is computed using the equation $\Phi = E_{vac} - E_f$ where E_{vac} and E_f are the energies of the vacuum level and the Fermi level, respectively, and it is found to be about 5 eV. Taking into account that, for the studied stack, $MoTe_2$ depletes electrons whereas $SnSe_2$ accumulates electrons, the heterostructure can be considered as an ultrathin parallel-plane capacitor, where a built-in electric field directed from $MoTe_2$ to $SnSe_2$ is formed. To quantify the spontaneous electron transfer, we perform a Bader charge analysis. Contrary to other charge analysis techniques like the one introduced by Mulliken or the one proposed by Löwdin [31,32], the Bader charge analysis conserves the total electron density [33]. Our simulations reveal that $\sim 2 \times 10^{13}$ electrons/cm^2 are transferred from $MoTe_2$ to $SnSe_2$ upon forming the heterostructure. Next, we compute the charge density difference using the equation $\Delta\rho_c = \rho(MoTe_2/SnSe_2) - \rho(MoTe_2) - \rho(SnSe_2)$, where $\rho(MoTe_2/SnSe_2)$, $\rho(MoTe_2)$, and $\rho(SnSe_2)$ are the charge densities of the heterostructure, the isolated $MoTe_2$ layer, and the isolated $SnSe_2$ layer, respectively. As expected, the charge transfer mainly occurs between the top-layer Te atoms and bottom-layer Se atoms, whereas $MoTe_2$ and $SnSe_2$ present electron depletion and accumulation, respectively.

For the sake of completeness, low-strained stacks with other rotation angles are also discussed. We consider heterostructures with relative rotations between the layers of $\sim$8, 10, 22, 24, and 26°, consisting of 165, 138, 156, 105, and

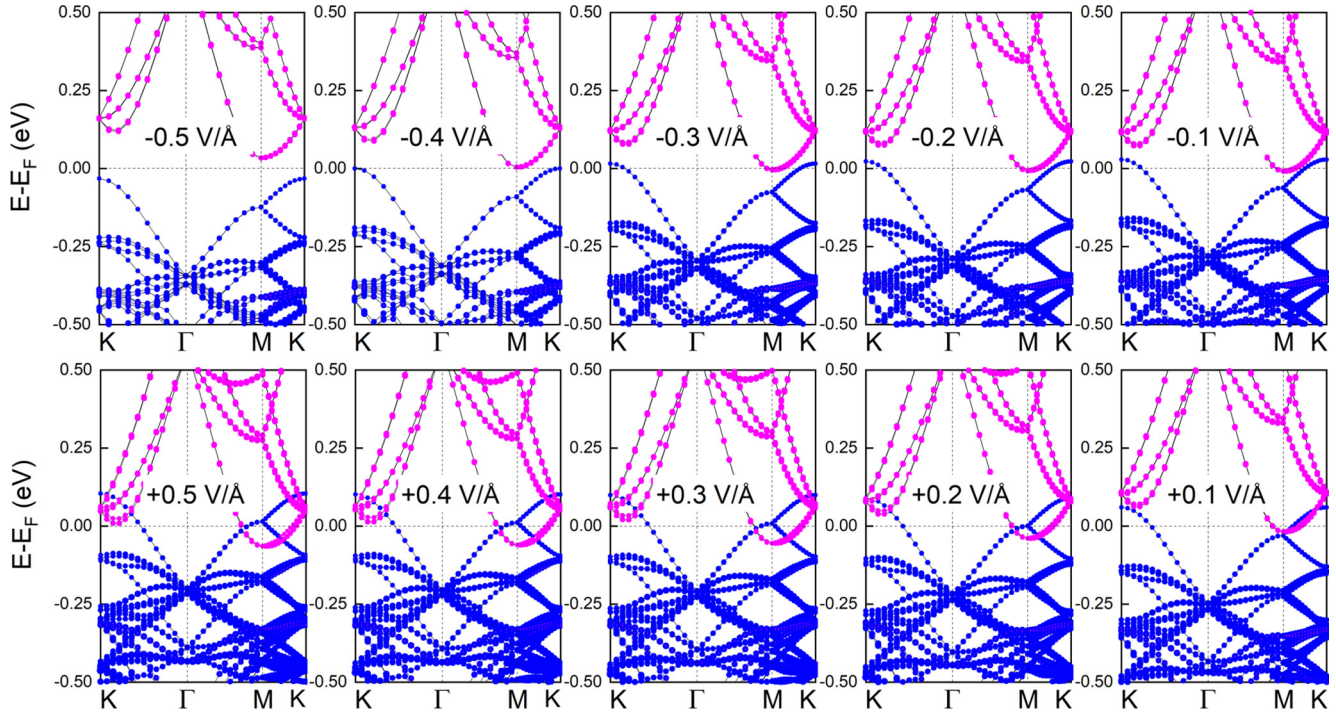

FIG. 3. Projected band structures at the PBE level with SOC of $MoTe_2/SnSe_2$ vdWHs under various external electric fields. The blue and pink lines correspond to contributions from the $MoTe_2$ and $SnSe_2$ layers, respectively.

129 total number of atoms, respectively (see Supplemental Material Fig. S1 [23]). Heterobilayers with rotation angles of 10 and 24° have hexagonal structures contrary to the other heterobilayers which exhibit oblique structures. Using PBE calculations, these stacks present the broken-gap band alignment similar to the 14°-rotated heterostructure (see Supplemental Material Fig. S2, Fig. S3, and Table S2 [23]).

For the sake of comparison, we also construct low-strained $WSe_2/SnSe_2$ heterobilayers where $SnSe_2$ is rotated by 30° and WSe_2 is kept fixed. Using PBE calculations with SOC, this heterostructure presents the broken-gap or type-III band alignment (see Supplemental Material Fig. S4 [23]), and we conclude that the $WSe_2/SnSe_2$ stack is also promising for realizing ultrathin tunneling transistors.

B. Effects of external electric field

To evaluate how the operating conditions affect the system, we examine the effect of an external electric field (E_{ext}) on the electronic properties of $MoTe_2/SnSe_2$ heterostructures. E_{ext} is applied in the out-of-plane direction, and positive values refer to an electric field directed from $MoTe_2$ to $SnSe_2$, whereas negative values refer to the opposite direction. The positive external electric field and the built-in electric field have the same orientation. Therefore, for $E_{ext} > 0$, the built-in electric field is enhanced, whereas the opposite behavior is observed for $E_{ext} < 0$. In our calculations, E_{ext} ranges from -0.5 to $0.5\,V/Å$, and a step of $0.05\,V/Å$ is used. Both relaxations and electronic structure calculations are performed in the presence of E_{ext}. Calculations where E_{ext} is considered only in the electronic structure calculations are also performed, leading to similar results. This confirms that the considered electric fields slightly affect the structural characteristics of $MoTe_2/SnSe_2$ vdWHs, which is also evident from the structural optimizations.

As shown in Fig. 3, by applying positive electric fields, $MoTe_2$ band-edge positions are shifted upward with respect to the Fermi level, whereas $SnSe_2$ band-edge positions are shifted downward. By increasing the positive electric field, the shifts of the band edges are also increased. Using PBE calculations with SOC and going from $E_{ext} = 0.2$ to $0.4\,V/Å$, the energy difference between the CB bottom originated from $SnSe_2$ and the VB top originated from $MoTe_2$ goes from -0.13 to $-0.16\,eV$. The lower the energy difference, the larger the energy window where the $MoTe_2$ high-lying VB states overlap with the $SnSe_2$ low-lying CB states. Consequently, more charge carriers are expected to tunnel from $MoTe_2$ to $SnSe_2$. On the other hand, by applying negative electric fields, the opposite behavior is observed. Calculations excluding SOC are also performed, and similar trends are observed (see Supplemental Material Fig. S5 [23]). For all applied electric fields, the energy difference between the CB bottom of $SnSe_2$ and the VB top of $MoTe_2$ using PBE calculations with SOC is shown in Fig. 4(a). Negative energy differences correspond to the broken-gap or type-III band alignment whereas positive values correspond to the staggered-gap or type-II band alignment.

Figure 4(b) presents the Bader charge transfer between the $MoTe_2$ and $SnSe_2$ layers under various external electric fields, and the results are further confirmed by computing the charge density differences (see Supplemental Material Fig. S6 [23]). As expected, for positive electric fields, the electron transfer from $MoTe_2$ to $SnSe_2$ increases, contrary to the results obtained for negative electric fields. Notably, the charge transfer is not fully symmetric with respect to the electric field direction and

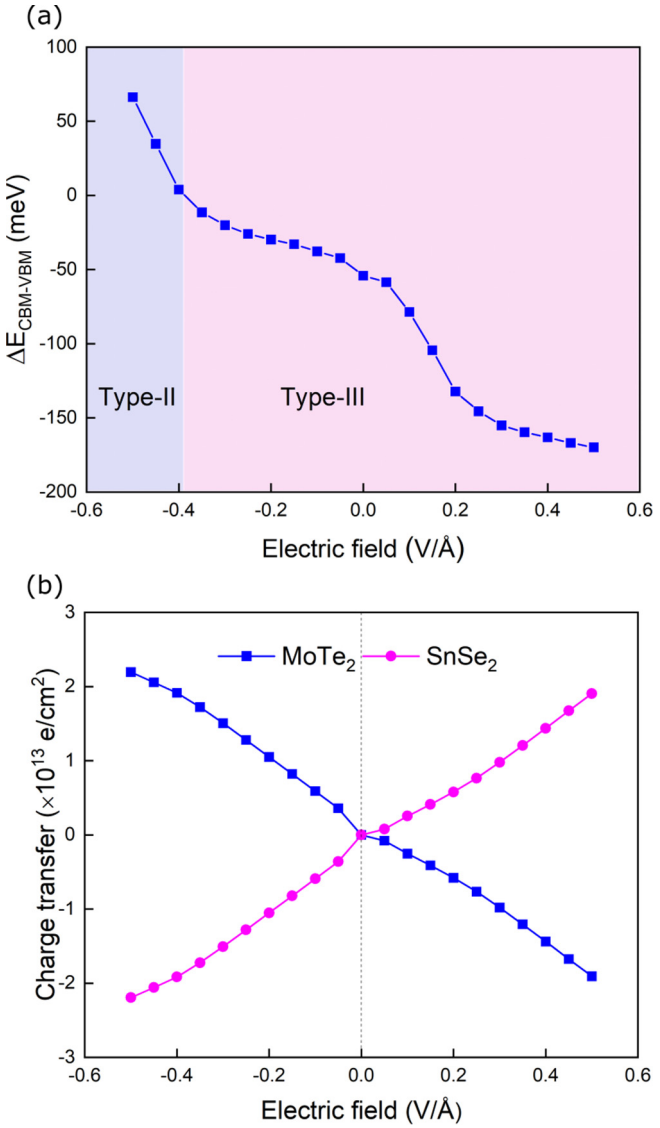

FIG. 4. (a) Energy difference between the CB bottom of $SnSe_2$ and the VB top of $MoTe_2$, and (b) Bader charge transfer between the $MoTe_2$ and $SnSe_2$ layers under various external electric fields, having as a reference the charge of the layers in the heterostructure with no electric field. The pink line corresponds to the charge transfer from $MoTe_2$ to $SnSe_2$. For both the energy differences and Bader charge transfers, SOC is included in the calculations.

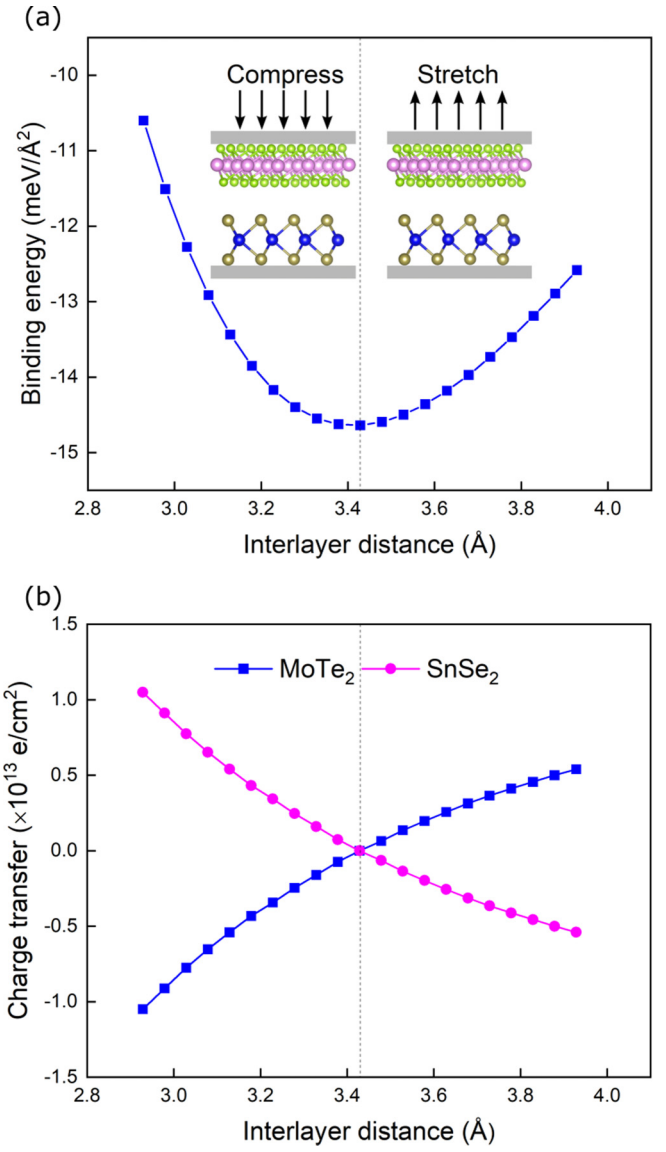

FIG. 5. (a) Binding energy and (b) Bader charge transfer between the $MoTe_2$ and $SnSe_2$ layers under various vertical strains, having as a reference the charge of the layers in the heterostructure with no strain. The pink line corresponds to the charge transfer from $MoTe_2$ to $SnSe_2$. For the Bader charge transfers, SOC is included in the calculations.

this finding agrees with previously reported theoretical calculations for heterostructures with the nearly broken-gap band alignment [34]. A different behavior has been reported for heterostructures with the staggered band alignment where the charge transfer was found to be symmetric [34].

C. Effects of strain

Strain engineering has been a standard strategy to tailor the electronic properties of 2D materials. Contrary to conventional bulk materials, 2D materials can tolerate large strain without fracture, and even small strains can modify their electronic properties [35]. Interestingly, atomic force microscopy (AFM) can be used not only to characterize 2D materials, but also to induce vertical pressure through contact between the AFM tip and the 2D material [35].

The interlayer distance, i.e., the distance between the highest top-layer Te atom and the lowest bottom-layer Se atom, is found to be 3.43 Å. Starting from the equilibrium structure, the interlayer distance is either increased or decreased up to 0.5 Å. Upon optimization, the bottom-layer Se atoms of $SnSe_2$ and the top-layer Te atoms of $MoTe_2$ are allowed to relax in the in-plane direction whereas all other atoms are allowed to relax fully. By modifying the interlayer distance, we examine the effect of the vertical strain on the electronic properties of the heterostructure.

As shown in Fig. 5(a), the binding energies of all studied strained configurations are negative, indicating their structural

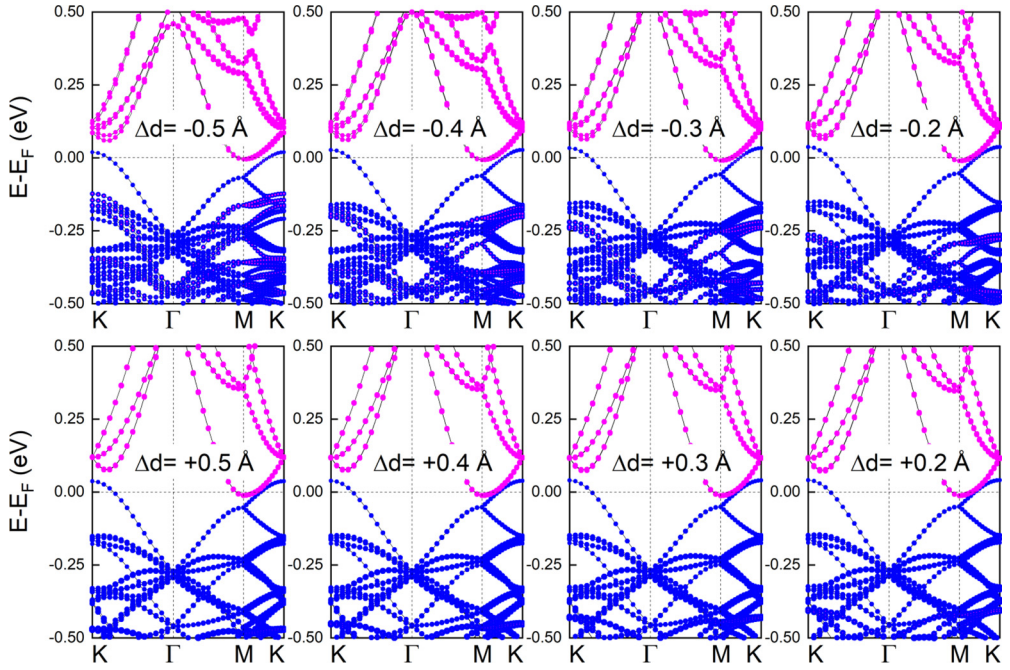

FIG. 6. Projected band structures at the PBE level with SOC of $MoTe_2/SnSe_2$ vdWHs under various vertical strains. The blue and pink lines correspond to contributions from the $MoTe_2$ and $SnSe_2$ layers, respectively. Δd refers to the variation of the interlayer distance, having as a reference the interlayer distance of the ground-state structure. Positive values of Δd refer to tensile strain whereas negative values refer to compressive strain.

stability. Figure 5(b) presents the Bader charge transfer between $MoTe_2$ and $SnSe_2$ under various vertical strains, and the results are further confirmed by computing the charge density differences (see Supplemental Material Fig. S7 [23]). Owing to the stronger coupling between the layers, the electron transfer from $MoTe_2$ to $SnSe_2$ increases for compressive strains, contrary to the results obtained for tensile strains. As shown in Fig. 6, for both types of deformation, no noticeable change in the position of the VB top of $MoTe_2$ and CB bottom of $SnSe_2$ in the k-space is observed, and the curvatures of the

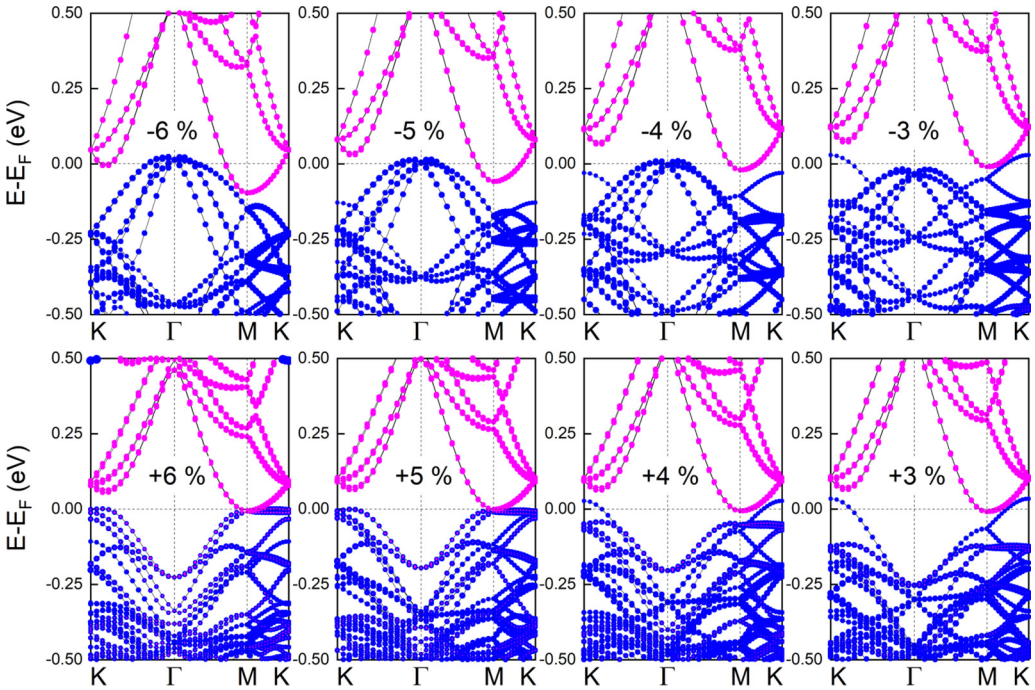

FIG. 7. Projected band structures at the PBE level with SOC of $MoTe_2/SnSe_2$ vdWHs under various in-plane biaxial strains. The blue and pink lines correspond to contributions from the $MoTe_2$ and $SnSe_2$ layers, respectively.

topmost VB and bottommost CB remain almost unaffected. Similar behavior is also found for calculations excluding SOC (see Supplemental Material Fig. S8 [23])

Besides the vertical strain, the effect of in-plane biaxial strain on the electronic properties of $MoTe_2/SnSe_2$ heterostructures is investigated. The biaxial strain is derived by $\varepsilon = (a - a_0)/a_0 \times 100\%$, where a and a_0 refer to the lattice constants of the strained and stain-free heterostructures, respectively, and positive and negative strain values correspond to tension and compression respectively. Upon optimization, the lattice parameters are fixed, whereas all atoms are allowed to relax fully. In line with the experiments [36], we consider configurations with up to 6% deformation. To evaluate whether the studied strains are within the elastic limit, we compute the strain energies using the equation $E_s = E_{\text{str}} - E_{\text{unstr}}$, where E_{str} and E_{unstr} are the total energies of the heterostructures with and without deformation, respectively. By increasing the strain, the corresponding strain energies are also increased. In addition, E_s variation has the form of a quadratic curve, indicating that the studied systems are within the range of elastic deformation (see Supplemental Material Fig. S9 [23]).

As shown in Fig. 7, upon application of compressive strains, the heterostructures present the broken-gap band alignment. For large compressive strains, the overlap between the high-lying valence states of $MoTe_2$ and the low-lying conduction states of $SnSe_2$ enhances, and more carriers can tunnel from $MoTe_2$ to $SnSe_2$, whereas the opposite behavior is observed for tensile strains. Notably, both types of deformation affect the position of the $MoTe_2$ VB maximum in the k-space. Similar behavior is also found for calculations excluding SOC (see Supplemental Material, Fig. S10 [23]).

IV. CONCLUSIONS

In this work, using density functional theory calculations, we examined the electronic properties of 2D $MoTe_2/SnSe_2$ heterostructures. Our calculations revealed that the heterostructure presents the nearly broken-gap or type-III band alignment, which is highly promising for TFET applications. We found that upon forming the heterostructure, $\sim 2 \times 10^{13}$ electrons/cm^2 spontaneously move from $MoTe_2$ to $SnSe_2$, and the heterostructure can be considered as an ultrathin plane capacitor with a built-in electric field directed from $MoTe_2$ to $SnSe_2$. In addition, our calculations showed that the band alignment can be tuned by applying external electric fields. For positive electric fields, $MoTe_2$ ($SnSe_2$) band-edge positions are shifted upward (downward) with respect to the Fermi level, and more electrons are expected to tunnel from $MoTe_2$ to $SnSe_2$. Accordingly, for large in-plane compressive strains, the overlap between the high-lying valence states of $MoTe_2$ and the low-lying conduction states of $SnSe_2$ enhances, leading to the increase in the tunneling current.

ACKNOWLEDGMENTS

The authors acknowledge funding from the "Area of Advance–Energy," the 2DTech Vinnova Competence Center at Chalmers, and the Gender Initiative for Excellence (Genie) at Chalmers University of Technology. The computations were performed on resources provided by the Swedish National Infrastructure for Computing (SNIC) at NSC, C3SE, and PDC.

[1] K. Bernstein, R. K. Cavin, W. Porod, A. C. Seabaugh, and J. Welser, Device and architectures outlook for beyond CMOS switches, Proc. IEEE **98**, 2169 (2010).

[2] A. C. Seabaugh and Q. Zhang, Low voltage tunnel transistors for beyond CMOS logic, Proc. IEEE **98**, 2095 (2010).

[3] A. M. Ionescu and H. Riel, Tunnel field-effect transistors as energy-efficient electronic switches, Nature (London) **479**, 329 (2011).

[4] X. Yan, C. Liu, C. Li, W. Bao, S. Ding, D. W. Zhang, and P. Zhou, Tunable $SnSe_2/WSe_2$ heterostructure tunneling field effect transistor, Small **13**, 1701478 (2017).

[5] J. Xu, J. Jia, S. Lai, J. Ju, and S. Lee, Tunneling field effect transistor integrated with black phosphorus−MoS_2 junction and ion gel dielectric, Appl. Phys. Lett. **110**, 033103 (2017).

[6] A. Nourbakhsh, A. Zubair, M. S. Dresselhaus, and T. Palacios, Transport properties of a MoS_2/WSe_2 heterojunction transistor and its potential for application, Nano Lett. **16**, 1359 (2016).

[7] X. Liu, D. Qu, H. M. Li, I. Moon, F. Ahmed, C. Kim, M. Lee, Y. Choi, J. H. Cho, J. C. Hone, and W. J. Yoo, Modulation of quantum tunneling via a vertical two-dimensional black phosphorus and molybdenum disulfide *p–n* junction, ACS Nano **11**, 9143 (2017).

[8] R. Yan, S. Fathipour, Y. Han, B. Song, S. Xiao, M. Li, N. Ma, V. Protasenko, D. A. Muller, and D. Jena, Esaki diodes in van der Waals heterojunctions with broken-gap energy band alignment, Nano Lett. **15**, 5791 (2015).

[9] G. Kresse and J. Furthmüller, Efficient iterative schemes for ab initio total-energy calculations using a plane-wave basis set, Phys. Rev. B **54**, 11169 (1996).

[10] G. Kresse and J. Furthmüller, Efficiency of ab initio total energy calculations for metals and semiconductors using a plane-wave basis set, Comput. Mater. Sci. **6**, 15 (1996).

[11] P. E. Blöchl, Projector augmented-wave method, Phys. Rev. B **50**, 17953 (1994).

[12] P. Lazić, CellMatch: Combining two unit cells into a common supercell with minimal strain, Comput. Phys. Commun. **197**, 324 (2015).

[13] I. Hamada, van der Waals density functional made accurate, Phys. Rev. B **89**, 121103(R) (2014).

[14] F. Tran, L. Kalantari, B. Traoré, X. Rocquefelte, and P. Blaha, Nonlocal van der Waals functionals for solids: Choosing an appropriate one, Phys. Rev. Materials **3**, 063602 (2019).

[15] J. Klimeš, D. R. Bowler, and A. Michaelides, van der Waals density functionals applied to solids, Phys. Rev. B **83**, 195131 (2011).

[16] M. Dion, H. Rydberg, E. Schröder, D. C. Langreth, and B. I. Lundqvist, van Der Waals Density Functional for General Geometries, Phys. Rev. Lett. **92**, 246401 (2004).

[17] G. Román-Pérez and J. M. Soler, Efficient Implementation of a Van Der Waals Density Functional: Application to Double-Wall Carbon Nanotubes, Phys. Rev. Lett. **103**, 096102 (2009).

[18] J. Klimeš, D. R. Bowler, and A. J. Michaelides, Chemical accuracy for the van der Waals density functional, J. Phys.: Condens. Matter **22**, 022201 (2009).

[19] K. Lee, E. D. Murray, L. Kong, B. I. Lundqvist, and D. C. Langreth, Higher-accuracy van der Waals density functional, Phys. Rev. B **82**, 081101(R) (2010).

[20] K. Berland and P. Hyldgaard, Exchange functional that tests the robustness of the plasmon description of the van der Waals density functional, Phys. Rev. B **89**, 035412 (2014).

[21] D. Puotinen and R. E. Newnham, The crystal structure of $MoTe_2$, Acta Crystallogr. **14**, 691 (1961).

[22] B. Pałosz and E. Salje, Lattice parameters and spontaneous strain in AX_2 polytypes: CdI_2, PbI_2, SnS_2 and $SnSe_2$, J. Appl. Crystallogr. **22**, 622 (1989).

[23] See Supplemental Material at http://link.aps.org/supplemental/10.1103/PhysRevMaterials.6.084001 for the crystalline lattice parameters using different van der Waals functionals, the atomic structures of heterostructures with various rotation angles, their band structures with and without SOC and the energy differences between the CB and VB edges, the atomic structure of $WSe_2/SnSe_2$ heterostructure and its band structure with SOC, the projected band structures for $MoTe_2/SnSe_2$ heterostructures without SOC under various external electric fields, vertical and in-plane biaxial strains, the charge density differences for different external electric fields and vertical strains, and the strain energies.

[24] J. P. Perdew, K. Burke, and M. Ernzerhof, Generalized Gradient Approximation Made Simple, Phys. Rev. Lett. **77**, 3865 (1996).

[25] J. Heyd, G. E. Scuseria, and M. Ernzerhof, Hybrid functionals based on a screened Coulomb potential, J. Chem. Phys. **118**, 8207 (2003).

[26] F. A. Rasmussen and K. S. Thygesen, Computational 2D materials database: Electronic structure of transition-metal dichalcogenides and oxides, J. Phys. Chem. C **119**, 13169 (2015).

[27] Z. Liu, J. Z. Liu, Y. Cheng, Z. Li, L. Wang, and Q. Zheng, Interlayer binding energy of graphite: A mesoscopic determination from deformation, Phys. Rev. B **85**, 205418 (2012).

[28] J. J. Zhou, W. Feng, C. C. Liu, S. Guan, and Y. Yao, Large-gap quantum spin hall insulator in single layer bismuth monobromide Bi_4Br_4, Nano Lett. **14**, 4767 (2014).

[29] C. Zhang, C. Gong, Y. Nie, K. A. Min, C. Liang, Y. J. Oh, H. Zhang, W. Wang, S. Hong, L. Colombo, and R. M. Wallace, Systematic study of electronic structure and band alignment of monolayer transition metal dichalcogenides in van der Waals heterostructures, 2D Mater. **4**, 015026 (2016).

[30] A. Rahman, H. J. Kim, M. Noor-A-Alam, and Y. H. Shin, A theoretical study on tuning band gaps of monolayer and bilayer SnS_2 and $SnSe_2$ under external stimuli, Curr. Appl. Phys. **19**, 709 (2019).

[31] P. O. Löwdin, On the non-orthogonality problem connected with the use of atomic wave functions in the theory of molecules and crystals, J. Chem. Phys. **18**, 365 (1950).

[32] R. S. Mulliken, Electronic population analysis on LCAO–MO molecular wave functions. I., J. Chem. Phys. **23**, 1833 (1955).

[33] R. F. Bader, Atoms in molecules, Acc. Chem. Res. **18**, 9 (1985).

[34] A. K. A. Lu, M. Houssa, I. P. Radu, and G. Pourtois, Toward an understanding of the electric field-induced electrostatic doping in van der Waals heterostructures: A first-principles study, ACS Appl. Mater. Interfaces **9**, 7725 (2017).

[35] S. Yang, Y. Chen, and C. Jiang, Strain engineering of two-dimensional materials: Methods, properties, and applications, InfoMat **3**, 397 (2021).

[36] C. R. Zhu, G. Wang, B. L. Liu, X. Marie, X. F. Qiao, X. Zhang, X. X. Wu, H. Fan, P. H. Tan, T. Amand, and B. Urbaszek, Strain tuning of optical emission energy and polarization in monolayer and bilayer MoS_2, Phys. Rev. B **88**, 121301(R) (2013).